Large Flux-Mediated Coupling in Hybrid Electromechanical System With A Transmon Qubit

Tanmoy Bera
Indian Institute of Science Bangalore
Sourav Majumder
Indian Institute of Science Bangalore
Sudhir Sahu
Indian Institute of Science Bangalore
Vibhor Singh (v.singh@iisc.ac.in)
Indian Institute of Science Bangalore https://orcid.org/0000-0002-9051-3867

Article

Keywords: quantum, oscillator, hybrid

Posted Date: November 9th, 2020

DOI: https://doi.org/10.21203/rs.3.rs-96050/v1

Version of Record: A version of this preprint was published at Communications Physics on January 19th, 2021. See the published version at https://doi.org/10.1038/s42005-020-00514-y.

Large flux-mediated coupling in hybrid electromechanical system with a transmon qubit

Tanmoy Bera,[1] Sourav Majumder,[1] Sudhir Kumar Sahu,[1] and Vibhor Singh[1,*]

[1]*Department of Physics, Indian Institute of Science, Bangalore-560012 (India)*

(Dated: October 21, 2020)

Abstract

Control over the quantum states of a massive oscillator is important for several technological applications and to test the fundamental limits of quantum mechanics. Addition of an internal degree of freedom to the oscillator could be a valuable resource for such control. Recently, hybrid electromechanical systems using superconducting qubits, based on electric-charge mediated coupling, have been quite successful. Here, we realize a hybrid device, consisting of a superconducting transmon qubit and a mechanical resonator coupled using the magnetic-flux. The coupling stems from the quantum-interference of the superconducting phase across the tunnel junctions. We demonstrate a vacuum electromechanical coupling rate up to 4 kHz by making the transmon qubit resonant with the readout cavity. Consequently, thermal-motion of the mechanical resonator is detected by driving the hybridized-mode with mean-occupancy well below one photon. By tuning qubit away from the cavity, electromechanical coupling can be enhanced to 40 kHz. In this limit, a small coherent drive on the mechanical resonator results in the splitting of qubit spectrum, and we observe interference signature arising from the Landau–Zener–Stückelberg effect. With improvements in qubit coherence, this system offers a novel platform to realize rich interactions and could potentially provide full control over the quantum motional states.

Cavity optomechanical systems, where a mechanical mode parametrically modulates the resonant frequency of an electromagnetic (EM) mode, have been very successful in controlling the motional states of massive oscillators [1]. Starting from the earlier demonstration of the motional quantum ground state by the sideband cooling technique [2, 3], these experiments have reached several milestones related to the displacement-detection [4] and the preparation of the non-classical states of mechanical motion [5, 6]. Beyond the traditional two-mode systems, consisting of one EM and one mechanical mode, cavity optomechanical systems with an auxiliary mode provides a wide range of interactions. Such systems have been used to realize nonreciprocal devices [7–9], and to demonstrate quantum entanglement between two mechanical resonators [10, 11].

Among the two-mode cavity optomechanical devices, preparation of the quantum states of motion appears to be technologically challenging. One successful strategy in the microwave domain, to circumvent this, is to introduce an auxiliary nonlinear mode such as a qubit. The qubit can be used as a single-photon source [12], photon-counter [13], or directly coupled to a mechanical mode using its charge dispersion [14–17] or the piezo-electric effect [18–20]. In such devices, the qubit mode 'acts' like an additional degree of freedom which couples to mechanical mode via an intermediate mode or directly using the "charge" dispersion.

While systems utilizing the charge-based coupling have been studied extensively, the experimental progress of the hybrid systems based on magnetic-flux has been very limited. Here we design and study the performance of a hybrid electromechanical device based on a fundamentally different coupling scheme based on the magnetic flux. We engineer the device parameters such that in addition to the flux-based electromechanical coupling, one mode maintains sufficient anharmonicity to be qualified as a qubit. This approach results in an electromechanical system with an internal spin-half degree of freedom. While, the strong and tunable nonlinearity of the qubit mode improves the displacement sensitivity, the large electromechanical coupling also manifests in the modification of qubit spectrum in the dispersive limit. Similar to vacuum-electromechanical coupling rate's scaling with total charge in charge-dispersion based schemes [14–16], the coupling rate with flux-based scheme is expected to scale linearly with the magnetic field. Therefore, such an approach has the potential to reach the elusive single-photon strong coupling regime with suitable choice of materials [21].

The hybrid device consists of a transmon qubit coupled to a mechanical resonator and a

readout cavity, as shown in Fig. 1(a). The transmon qubit couples to the cavity via a dipole coupling, commonly referred to as transverse coupling, as it connects the ground and the first excited state of the qubit [22]. The mechanical resonator couples to the qubit via a flux-mediated coupling. Such coupling is achieved by embedding a mechanical resonator into one of the arms of a SQUID (Superconducting Quantum Interference Device) loop, which provides the necessary Josephson inductance to form a transmon qubit. Due to the quantum interference of the superconducting phase, the Josephson inductance of the SQUID depends on the magnetic flux threading the loop as schematically shown in Fig. 1(b). In the presence of a magnetic field applied normal to the plane of the SQUID, it acts like a displacement-dependent nonlinear inductor. By shunting the SQUID "inductor" to a suitable capacitance, a transmon qubit mode can be designed. As the motion of the mechanical resonator directly affects the qubit transition frequency, this coupling is referred to as longitudinal coupling. A flux-coupled hybrid system formed this way can be thought of a dual to the "charge" coupling approach realized with the CPB qubit [16].

Theoretically, the flux-mediated electromechanical coupling has been considered in the context of flux-qubits [23], cavity-electromechanical devices [24], and more recently with the transmon qubit [21, 25]. On the experimental side, the scheme has been used for large bandwidth displacement detection [26], and to demonstrate the cavity-electromechanical system by embedding Josephson elements in the microwave circuitry [27, 28].

In comparison to existing flux-coupling approaches[27, 28], our design methodology circumvents several issues by using a tunable transmon-mode. First, the requirement of large Josephson inductance for transmon design helps in suppressing hysteretic effects with magnetic flux arising from geometrical and kinetic inductance. Second, our approach here is to implement a longitudinal coupling between transmon qubit and a mechanical resonator through the modulation of Josephson inductance. This enables the interaction of the mechanical mode with the qubit in two distinct ways. First, due to strong coupling between the qubit and cavity in the resonant limit, the mechanical motion directly couples to the hybridized-states. Second, in the dispersive limit when the qubit is detuned far away from the cavity, a sufficiently large coupling between the qubit and the mechanical mode can be maintained. It thus provides a mean to use the qubit as an internal degree of freedom to the mechanical mode and further paves ways for measurement-based cooling and control protocols [25, 29, 30].

Device design

We use a three-dimensional (3D) cavity to implement the transmon design as shown schematically in Fig. 1(c). Unlike the conventional 3D-transmon qubit, which couples differentially to the cavity mode, we design a single-ended qubit mode by grounding one end of the SQUID loop to the cavity wall using a small wirebond [31]. The other end of the SQUID loop extends towards the center of the cavity and provides the necessary qubit capacitance and coupling with the fundamental cavity mode. The rectangular cavity ($35\times4\times35$ mm^3) is machined using OFHC copper with the fundamental resonant mode TE_{101} at $\omega_c \approx 2\pi\times$ 6 GHz. A false-color SEM image of the SQUID loop is shown in Fig. 1(d). The nanobeam-shaped mechanical resonator, formed by 100 nm highly-stressed SiN film coated with 50 nm of Aluminum, and suspended part of the Josephson junctions can be clearly seen. See supplementary information (SI) for details. The offset in the SQUID position (away from the center of the cavity) in transmon design allows us to bring a RF drive line for the electrostatic actuation of the mechanical resonator (see SI for design simulations).

The transmon qubit frequency ω_q is given by $\hbar\omega_q \approx \sqrt{8E_C E_J^0 \left|\cos\left(\pi\Phi/\Phi_0\right)\right|} - E_C$, where E_J^0 is the maximum Josephson energy, E_C is the charging energy, Φ is the total flux threading the SQUID loop, and $\Phi_0 = h/2e$ is the magnetic flux quanta. The tunability of qubit frequency with flux allows access to its dispersive or resonant interaction with the cavity. The interaction between the qubit and the cavity mode can be expressed as $\hbar J(\hat{a}\hat{\sigma}^+ + \hat{a}^\dagger\hat{\sigma}^-)$, where $\hat{a}(\hat{\sigma}^-)$ is the ladder operator for the cavity(qubit) mode and J is the dipole coupling rate. The electromechanical coupling arises from the modulation of qubit frequency caused by mechanical displacement. As the qubit frequency can be tuned over a large range, it is convenient to define the vacuum electromechanical coupling rate between the qubit-cavity hybridized states ($\omega_\pm$) and the mechanical resonator as,

$$g_\pm(\Phi) = \frac{\partial\omega_\pm(\Phi)}{\partial x} x_{zp} = \Phi G_\Phi^\pm \frac{x_{zp}}{w}, \tag{1}$$

where $G_\Phi^\pm = \partial\omega_\pm(\Phi)/\partial\Phi$ is the flux-responsivity, x_{zp} is the quantum zero-point fluctuations of the mechanical resonator, and w is the effective width of the SQUID loop. Eq. 1 defines the coupling rate over the entire range of qubit frequencies. The hybridized modes $\omega_\pm = \bar{\Delta} \pm \sqrt{(\Delta/2)^2 + J^2}$ with $\Delta = \omega_q - \omega_c$ $\bar{\Delta} = \left(\omega_q + \omega_c\right)/2$ approach the uncoupled qubit and cavity frequencies in the dispersive limit. Restricting the coupled qubit-cavity system to single excitation subspace, in the resonant limit $\Delta \ll J$, the hybridized-modes essentially

act like independent cavity optomechanical systems. However, it is worth pointing out here that the interaction between the hybridized modes and the mechanical motion can be used to enhance the quantum nonlinearity by designing Jcomparable to the mechanical frequency [32, 33].

Qubit spectroscopy and flux-responsivity

We use spectroscopic measurements to characterize the qubit. Fig. 2(a) shows the transmission ($|S_{21}(\omega)|$) through the cavity as applied magnetic flux is varied (see SI for details of the measurement setup). When the qubit becomes resonant with the cavity, the vacuum Rabi splitting is observed which signifies the strong coupling between the qubit and cavity mode. We determine a dipole coupling rate $J = 2\pi\times85$ MHz, the bare cavity frequency $\omega_c = 2\pi\times5.993$ GHz, maximum qubit frequency $\omega_q^0 = 2\pi\times7.982$ GHz, and an anharmonicity of -132 MHz (see SI for details). Due to the flux-periodicity of qubit frequency, the vacuum-Rabi splitting pattern repeats with every new flux-quanta added. The extension panel of Fig. 2(a) shows the transmission measurement at a higher magnetic field. Apart from a small reduction ($\sim$15 MHz) in the maximum qubit frequency and an increase in the dressed-cavity mode linewidth, we do not observe any significant change in the device parameters up to a field of $\sim$ 3.7 mT (310 Φ_0).

To understand the flux-transduction of hybridized-modes, we compute the flux-responsivity $G_\Phi^\pm$ using the measured qubit and cavity parameters and assuming identical junctions. Fig. 2(b) shows the plot of $G_\Phi^\pm$ with respect to the hybridized-mode frequencies. The flux-responsivity of the hybridized-modes increase as their relative detuning ($|\omega_\pm - \omega_c|$) increases. However, reduced transmission at frequencies far away from ω_c hinders their use for the mechanical transduction. We choose an optimum operating point of 6.025 GHz, corresponding to $G_\Phi^+/2\pi \sim$1.8 GHz/Φ_0, for the mechanical resonator characterization. This flux-responsivity is significantly larger than the values reported with the SQUID cavity [27]. In addition, the flux-responsivity of qubit $G_\Phi^q = \partial\omega_q/\partial\Phi$ can be much larger near the half-integer flux quantum as shown in Fig. 2(c). In the dispersive limit, while the effective coupling between the dressed cavity and mechanical resonator degrades by a factor of $(J/\Delta)^2$, a large coupling between the qubit and the mechanical resonator can be maintained.

Detection of mechanical mode and vacuum electromechanical rate

We first focus on the driven response of the mechanical resonator. For electrostatic actuation, a weak ac signal and a dc voltage V_{dc} are applied at the mechanical drive port (see SI for details). We fine-tune the magnetic flux near 190 Φ_0 to operate the hybridized mode $\omega_+/2\pi$ at 6.025 GHz. We inject a microwave tone at ω_+ creating a mean photon occupation of ≈ 1, calibrated independently using ac-Stark shift. The signal that emerges from the cavity is then mixed-down and recorded by a network analyzer. Fig. 3(a) shows the amplitude of the signal in a color plot as the mechanical drive frequency and V_{dc} are varied. The change in color over the background signifies the mechanical resonance. We measure the in-plane vibrational mode at $\omega_m \sim 2\pi\times 6.585$ MHz with a characteristic capacitive frequency softening with V_{dc}.

Next, we focus on the thermal motion of the mechanical resonator. We operate the hybridized mode at $\omega_+ = 2\pi\times$ 6.025 GHz and drive the system with a microwave tone tuned to lower sideband $(\omega_+ - \omega_m)$, creating a mean photon occupation of ~ 0.1 photons. The power spectral density (PSD) of the output signal is then recorded with a spectrum analyzer. The average PSD, along with the fitted Lorentzian is shown in Fig. 3(b). We measure a mechanical linewidth of $\gamma_m = 2\pi\times 6$ Hz, corresponding to a quality factor of $\sim 1.1\times 10^6$.

For a drive at the lower sideband, the ratio of integrated power at the up-converted frequency (P_m) near ω_+ to the power of transmitted carrier signal (P_d) at $\omega_+ - \omega_m$ can be conveniently expressed as $P_m/P_d = (2g_+/\kappa)^2\, n_m^{th}$, where n_m^{th} is the mean thermal occupation of the mechanical mode, and κ is the hybridized-mode linewidth. By varying the fridge temperature, we estimated the mechanical mode to be thermalized to at least 50 mK or higher. For the calculation of g_+, we use a thermal phonon occupancy of 169 corresponding to 53 mK (additional detail are given in SI). Fig. 3(c) shows the variation in g_+ as the magnetic flux through the SQUID loop is varied, while the hybridized-mode frequency is maintained fixed at $\omega_+/2\pi = 6.025$ GHz. The dotted line shows the expected electromechanical coupling rate estimated from Eq. 1 using the measured device parameters.

We emphasize that the vacuum electromechanical coupling rate of $g_+ \sim 2\pi\times 4$ kHz is limited by choice of ω_+, and the magnetic field range available in our measurement setup. By operating at $\omega_c \pm J$, one can achieve the $G_\Phi^+/G_\Phi^q = 1/2$, resulting in $g_+ \sim 2\pi\times 15$ kHz.

In addition, thin films of Al can withstand a larger magnetic field than the maximum field used here (3.7 mT). As the in-plane critical magnetic field is much larger than the perpendicular critical magnetic field for thin Al films, a configuration with field applied in-plane to the SQUID loop would result in significantly higher coupling rates for the out-of-plane mechanical mode.

Landau-Zener-Stückelberg interference in the dispersive limit

Next, we investigate the system by tuning the qubit away from ω_c. In the dispersive limit $|\Delta| \gg J$, the mechanics essentially decouples from the cavity mode. While the qubit-cavity interaction is given by $(J^2/\Delta)\,\hat{a}^\dagger\hat{a}\hat{\sigma}_z$, the longitudinal interaction between the uncoupled qubit and the mechanical resonator is given by $g_{qm}\hat{\sigma}_z(\hat{b}+\hat{b}^\dagger)$, where $g_{qm} = (\partial\omega_q/\partial x)\,x_{zp}$ is the qubit-electromechanical coupling rate and $\hat{b}$ ($\hat{b}^\dagger$) is the lowering (raising) operator for the mechanical mode. With a superconducting qubit device, time-dependent longitudinal coupling scheme has been used to perform high-fidelity qubit measurements [34]. In the present device, a static g_{qm} would instead result in a small qubit-state dependent displacement ($\sim g_{qm}x_{zp}/\omega_m$) [29]. Here, we focus on the qubit dynamics while driving the mechanical resonator. The qubit is detuned to 4.9 GHz to enhance g_{qm} to 40 kHz, and its spectrum is probed using the two-tone spectroscopy technique. The mechanical resonator is coherently actuated at its resonant frequency. It is equivalent to the flux-modulation of the qubit frequency at ω_m, and a frequency deviation set by g_{qm} and the mechanical amplitude.

Fig. 4(a) shows the qubit spectrum as the strength of mechanical drive is varied. We observe a splitting in the qubit spectrum with a weak modulation in-between. The separation between the primary splitting varies linearly with the mechanical amplitude. The primary splitting can be understood by considering the passage of the system across the region of avoided crossing with separation set by the strength of the spectroscopic tone (the Rabi-flop rate Ω_R) [35]. As the system moves across the avoided-crossing at a rate set by ω_m, the transition during multiple passages mix the two states, eventually resulting in almost equal population of the two energy levels. Hence, it results in the splitting of the qubit spectrum.

At large mechanical drive power, the system crosses avoided-crossing region with higher speed. In this regime, one would expect to see the interference fringes, arising from multiple Landau-Zener transitions, at a separation close to ω_m [35] (additional details are included in

the SI). In our experiment, as the qubit linewidth is comparable to the modulation frequency ω_m, the fringes are not well resolved. Their signatures are visible as weak modulation between the primary splitting. We have performed numerical calculations based on the Lindblad master equation (details are included in SI). Fig. 4(b) shows the result from such calculations. Apart from capturing the linear amplitude dependence of the primary splitting, the calculated results show the weak modulation in the experimental data.

In summary, we have developed a hybrid electromechanical device by integrating a modified 3D-transmon qubit and extremely low loss mechanical resonator of SiN/Al. The detection of thermo-mechanical motion by driving the system with less than one photon highlights the large underlying coupling rate. Accessibility to different regimes of interaction is further demonstrate by the observation of the LZS interference. Looking ahead, by accessing in-plane vibration mode through changes in the design geometry and in combination with higher magnetic field, the flux coupling rate can be increased a lot. With further improvements in the coupling strength, the device in consideration can reach resolved sideband regime and strong coupling regime. This could enable experiments in the regime of the single-photon cooperativity exceeding one, and a conditional cooling of the mechanical resonator to the quantum ground state.

Methods

For device fabrication, we use an intrinsic Si (100) substrate coated with 100 nm thick high-stress SiN layer grown using the LPCVD method. Using standard lithography and shadow evaporation techniques, the transmon design is patterned in a single lithography step. To release the mechanical resonator, a combination of dry and wet etching processes is used. First, the exposed SiN is vertically etched by the reactive ion etching using SF_6 and CHF_3 plasma. The aluminum film naturally acts as a mask layer and thus protects the SiN underneath it. In the second step of etching, a modified-TMAH based etchant is used to remove the exposed silicon, while providing excellent selectivity against Al and SiN (see SI for additional details). After the wet etch process, the samples are blow-dried gently with N_2, requiring no critical point drying. The (111)-facets of Si resulted from the wet etch process can also be seen in Fig. 1(d). The sample placed inside a copper cavity, along with a small solenoid, is kept inside a cryoperm-shield to protect it from the ambient magnetic

field fluctuations.

Acknowledgments

V.S. acknowledges the support received from Infosys Science Foundation, and under the "Early Career Research Award" by SERB, Department of Science and Technology (DST), Govt. of India. T. B. and S. M. thank Tata Trust for providing the travel support. The authors acknowledge device fabrication facilities at CeNSE, IISc, Bangalore, and central facilities at the Department of Physics funded by DST. Authors thank R. Vijayraghavan, Manas Kulkarni, Diptiman Sen, and G. S. Agarwal for valuable discussions.

Author contribution

T. B. and S. M. contributed equally to this work. V. S. conceived the experiments. T. B. and S. M. fabricated the devices. T. B., S. M. and S. K. S performed the measurements. T. B., S. M., and V. S. performed data analysis. All the authors contributed to write the manuscript and discuss the results.

Competing interests

The authors declare no competing interests.

Data availability

All raw data and processed data as well as supporting code for processing and figure generation is available in Zenodo with the identifier (URL will be inserted at the time of publication).

* v.singh@iisc.ac.in

[1] Markus Aspelmeyer, Tobias J. Kippenberg, and Florian Marquardt, "Cavity optomechanics," Reviews of Modern Physics **86**, 1391–1452 (2014).

[2] J. D. Teufel, T. Donner, Dale Li, J. W. Harlow, M. S. Allman, K. Cicak, A. J. Sirois, J. D. Whittaker, K. W. Lehnert, and R. W. Simmonds, "Sideband cooling of micromechanical motion to the quantum ground state," Nature **475**, 359–363 (2011).

[3] Jasper Chan, T. P. Mayer Alegre, Amir H. Safavi-Naeini, Jeff T. Hill, Alex Krause, Simon Gröblacher, Markus Aspelmeyer, and Oskar Painter, "Laser cooling of a nanomechanical oscillator into its quantum ground state," Nature **478**, 89–92 (2011).

[4] G. Anetsberger, E. Gavartin, O. Arcizet, Q. P. Unterreithmeier, E. M. Weig, M. L. Gorodetsky, J. P. Kotthaus, and T. J. Kippenberg, "Measuring nanomechanical motion with an imprecision below the standard quantum limit," Physical Review A **82**, 061804 (2010).

[5] J.-M. Pirkkalainen, E. Damskägg, M. Brandt, F. Massel, and M.A. Sillanpää, "Squeezing of Quantum Noise of Motion in a Micromechanical Resonator," Physical Review Letters **115**, 243601 (2015).

[6] E. E. Wollman, C. U. Lei, A. J. Weinstein, J. Suh, A. Kronwald, F. Marquardt, A. A. Clerk, and K. C. Schwab, "Quantum squeezing of motion in a mechanical resonator," Science **349**, 952–955 (2015).

[7] G.A. Peterson, F. Lecocq, K. Cicak, R.W. Simmonds, J. Aumentado, and J.D. Teufel, "Demonstration of Efficient Nonreciprocity in a Microwave Optomechanical Circuit," Physical Review X **7**, 031001 (2017).

[8] N. R. Bernier, L. D. Tóth, A. Koottandavida, M. A. Ioannou, D. Malz, A. Nunnenkamp, A. K. Feofanov, and T. J. Kippenberg, "Nonreciprocal reconfigurable microwave optomechanical circuit," Nature Communications **8**, 604 (2017).

[9] S. Barzanjeh, M. Wulf, M. Peruzzo, M. Kalaee, P. B. Dieterle, O. Painter, and J. M. Fink, "Mechanical on-chip microwave circulator," Nature Communications **8**, 1–7 (2017).

[10] Ralf Riedinger, Andreas Wallucks, Igor Marinković, Clemens Löschnauer, Markus Aspelmeyer, Sungkun Hong, and Simon Gröblacher, "Remote quantum entanglement between two micromechanical oscillators," Nature **556**, 473–477 (2018).

[11] C. F. Ockeloen-Korppi, E. Damskägg, J.-M. Pirkkalainen, M. Asjad, A. A. Clerk, F. Massel, M. J. Woolley, and M. A. Sillanpää, "Stabilized entanglement of massive mechanical oscillators," Nature **556**, 478–482 (2018).

[12] A. P. Reed, K. H. Mayer, J. D. Teufel, L. D. Burkhart, W. Pfaff, M. Reagor, L. Sletten, X. Ma, R. J. Schoelkopf, E. Knill, and K. W. Lehnert, "Faithful conversion of propagating

quantum information to mechanical motion," Nature Physics **13**, 1163–1167 (2017).

[13] F. Lecocq, J. D. Teufel, J. Aumentado, and R. W. Simmonds, "Resolving the vacuum fluctuations of an optomechanical system using an artificial atom," Nature Physics **11**, 635–639 (2015).

[14] J.-M. Pirkkalainen, S. U. Cho, Jian Li, G. S. Paraoanu, P. J. Hakonen, and M. A. Sillanpää, "Hybrid circuit cavity quantum electrodynamics with a micromechanical resonator," Nature **494**, 211–215 (2013).

[15] J.-M. Pirkkalainen, S.U. Cho, F. Massel, J. Tuorila, T.T. Heikkilä, P.J. Hakonen, and M.A. Sillanpää, "Cavity optomechanics mediated by a quantum two-level system," Nature Communications **6** (2015), 10.1038/ncomms7981.

[16] J.J. Viennot, X. Ma, and K.W. Lehnert, "Phonon-Number-Sensitive Electromechanics," Physical Review Letters **121**, 183601 (2018).

[17] L. R. Sletten, B. A. Moores, J. J. Viennot, and K. W. Lehnert, "Resolving phonon fock states in a multimode cavity with a double-slit qubit," Phys. Rev. X **9**, 021056 (2019).

[18] A. D. O'Connell, M. Hofheinz, M. Ansmann, Radoslaw C. Bialczak, M. Lenander, Erik Lucero, M. Neeley, D. Sank, H. Wang, M. Weides, J. Wenner, John M. Martinis, and A. N. Cleland, "Quantum ground state and single-phonon control of a mechanical resonator," Nature **464**, 697–703 (2010).

[19] Yiwen Chu, Prashanta Kharel, Taekwan Yoon, Luigi Frunzio, Peter T. Rakich, and Robert J. Schoelkopf, "Creation and control of multi-phonon Fock states in a bulk acoustic-wave resonator," Nature **563**, 666 (2018).

[20] Patricio Arrangoiz-Arriola, E. Alex Wollack, Zhaoyou Wang, Marek Pechal, Wentao Jiang, Timothy P. McKenna, Jeremy D. Witmer, Raphael Van Laer, and Amir H. Safavi-Naeini, "Resolving the energy levels of a nanomechanical oscillator," Nature **571**, 537–540 (2019).

[21] Marios Kounalakis, Yaroslav M. Blanter, and Gary A. Steele, "Flux-mediated optomechanics with a transmon qubit in the single-photon ultrastrong-coupling regime," Physical Review Research **2** (2020).

[22] Jens Koch, Terri M. Yu, Jay Gambetta, A. A. Houck, D. I. Schuster, J. Majer, Alexandre Blais, M. H. Devoret, S. M. Girvin, and R. J. Schoelkopf, "Charge-insensitive qubit design derived from the Cooper pair box," Physical Review A **76**, 042319 (2007).

[23] Fei Xue, Y. D. Wang, C. P. Sun, H. Okamoto, H. Yamaguchi, and K. Semba, "Controllable coupling between flux qubit and nanomechanical resonator by magnetic field," New Journal of Physics **9**, 35–35 (2007).

[24] P. D. Nation, J. Suh, and M. P. Blencowe, "Ultrastrong optomechanics incorporating the dynamical Casimir effect," Physical Review A **93**, 022510 (2016).

[25] K.E. Khosla, M.R. Vanner, N. Ares, and E.A. Laird, "Displacemon Electromechanics: How to Detect Quantum Interference in a Nanomechanical Resonator," Physical Review X **8**, 021052 (2018).

[26] S. Etaki, M. Poot, I. Mahboob, K. Onomitsu, H. Yamaguchi, and H. S. J. van der Zant, "Motion detection of a micromechanical resonator embedded in a d.c. SQUID," Nature Physics **4**, 785–788 (2008).

[27] I. C. Rodrigues, D. Bothner, and G. A. Steele, "Coupling microwave photons to a mechanical resonator using quantum interference," Nature Communications **10** (2019).

[28] Philip Schmidt, Mohammad T. Amawi, Stefan Pogorzalek, Frank Deppe, Achim Marx, Rudolf Gross, and Hans Huebl, "Sideband-resolved resonator electromechanics on the single-photon level based on a nonlinear Josephson inductance," arXiv:1912.08731 [cond-mat, physics:quant-ph] (2019), arXiv: 1912.08731.

[29] Nicolas Didier, Jérôme Bourassa, and Alexandre Blais, "Fast Quantum Nondemolition Readout by Parametric Modulation of Longitudinal Qubit-Oscillator Interaction," Physical Review Letters **115**, 203601 (2015).

[30] D. Leibfried, R. Blatt, C. Monroe, and D. Wineland, "Quantum dynamics of single trapped ions," Reviews of Modern Physics **75**, 281–324 (2003).

[31] R. Barends, J. Kelly, A. Megrant, D. Sank, E. Jeffrey, Y. Chen, Y. Yin, B. Chiaro, J. Mutus, C. Neill, P. O'Malley, P. Roushan, J. Wenner, T. C. White, A. N. Cleland, and John M. Martinis, "Coherent Josephson Qubit Suitable for Scalable Quantum Integrated Circuits," Physical Review Letters **111**, 080502 (2013).

[32] Max Ludwig, Amir H. Safavi-Naeini, Oskar Painter, and Florian Marquardt, "Enhanced Quantum Nonlinearities in a Two-Mode Optomechanical System," Physical Review Letters **109**, 063601 (2012).

[33] Lev S. Bishop, J. M. Chow, Jens Koch, A. A. Houck, M. H. Devoret, E. Thuneberg, S. M. Girvin, and R. J. Schoelkopf, "Nonlinear response of the vacuum Rabi resonance," Nature

Physics **5**, 105–109 (2009).

[34] S. Touzard, A. Kou, N.E. Frattini, V.V. Sivak, S. Puri, A. Grimm, L. Frunzio, S. Shankar, and M.H. Devoret, "Gated Conditional Displacement Readout of Superconducting Qubits," Physical Review Letters **122**, 080502 (2019).

[35] S. N. Shevchenko, S. Ashhab, and Franco Nori, "Landau–Zener–Stückelberg interferometry," Physics Reports **492**, 1–30 (2010).

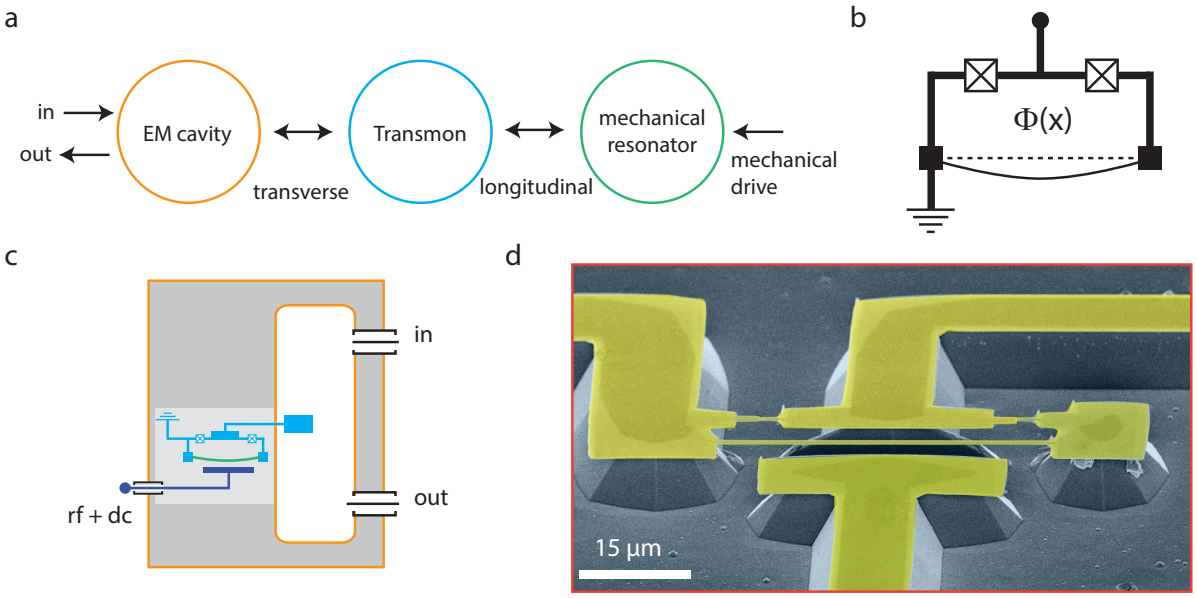

FIG. 1. (a) A schematic showing various components of the hybrid electromechanical system. The transmon qubit couples to an electromagnetic (EM) cavity via the transverse coupling. A low-frequency mechanical resonator couples to the transmon qubit via the longitudinal coupling. (b) A schematic of the SQUID loop with a suspended arm. Due to the magnetic flux $\Phi(x)$ dependence of Josephson inductance, it forms a displacement-dependent inductor. (c) A cross-sectional view of a 3D-cavity based transmon device. The gray (white) portion represents the copper (machined chamber). Input-output ports for microwave and a third port added for mechanical actuation is shown. The SQUID loop is placed inside a small recess of the cavity schematically shown by the lighter gray area. (d) A false-color SEM image of the SQUID loop, showing the suspended portion of the Josephson junctions and the nanobeam. The mechanical resonator has a length and width of 45 μm and 300 nm, respectively. It consists of a 50 nm coating of aluminum over 100 nm thick highly-stressed SiN film. The T-shaped electrode in the lower-half of the image is used to actuate the mechanical resonator.

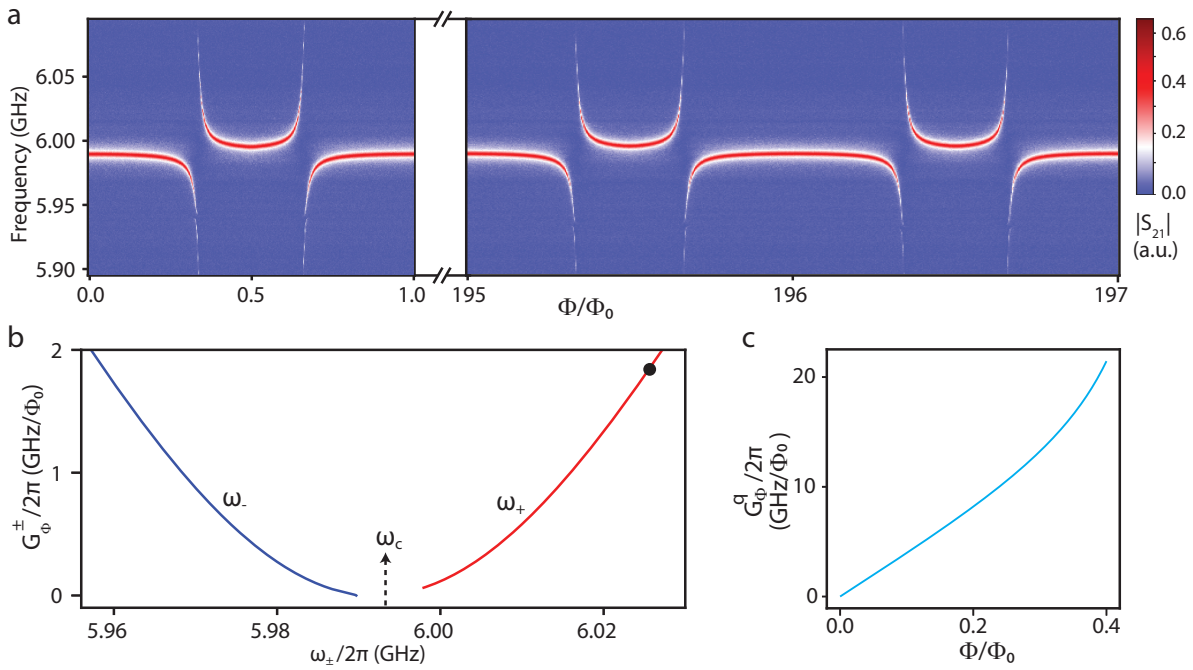

FIG. 2. (a) Color scale plot of transmission $|S_{21}|$ through the cavity as the magnetic flux through the SQUID loop is varied. The strong qubit-cavity coupling (J) manifests as the avoided-crossing, yielding $J \sim 2\pi \times 85$ MHz. The extension panel shows the trend of avoided crossing at larger values of the magnetic flux. (b) The flux-responsivity $G_\Phi^\pm = \partial\omega_\pm/\partial\Phi$, computed using the measured device parameters, assuming identical junctions, plotted as a function of hybridized frequencies. The black dot denotes the operating point of 6.025 GHz, corresponding to $G_\Phi^+/2\pi \sim$1.8 GHz/Φ_0 for the subsequent measurements. The arrow indicates the bare cavity frequency $\omega_c/2\pi \sim$5.993 GHz. Panel (c) shows the flux-responsivity of uncoupled qubit $G_\Phi^q = \partial\omega_q/\partial\Phi$ with the magnetic flux.

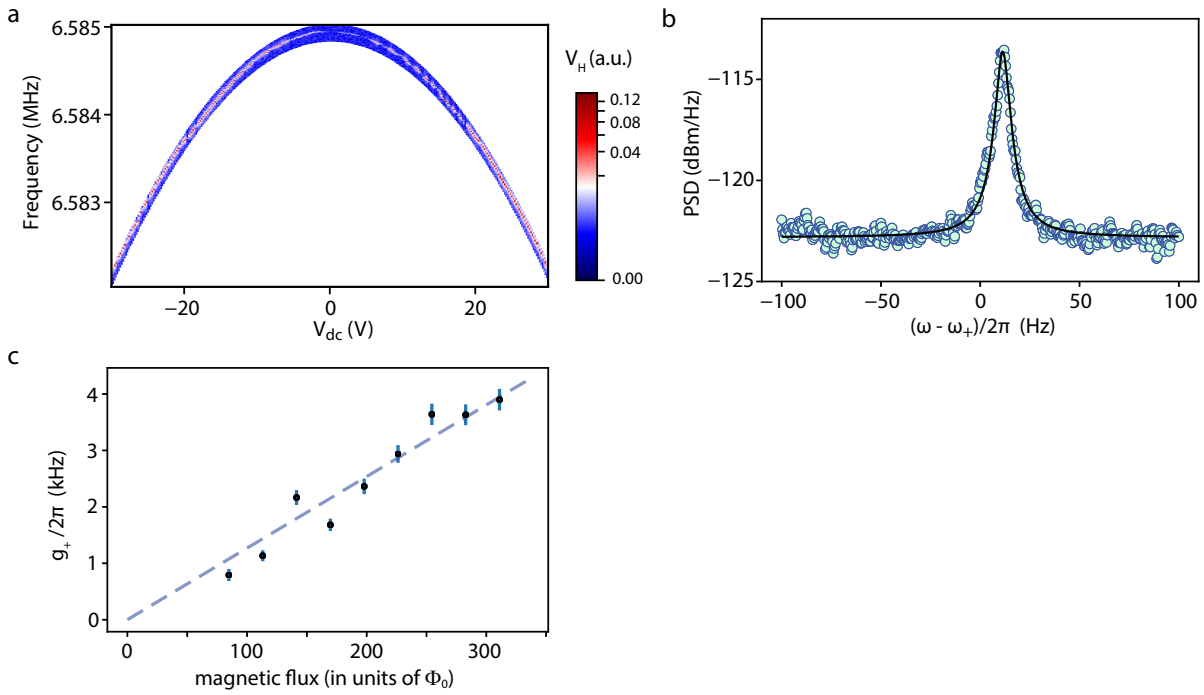

FIG. 3. (a) Color plot of the mixed-down signal V_H as mechanical actuation frequency and dc voltage is varied. The mechanical resonance appears as a sharp change in the color. Blue(red) color represents low(high) values of the signal. To reduce the total measurement time, the mechanical actuation frequency range is automatically adjusted to follow the mechanical mode. (b) Average PSD along with a fitted curve yielding a mechanical linewidth $\gamma_m \sim 2\pi \times 6$ Hz corresponding to a quality factor of $\sim 1.1 \times 10^6$. (c) Plot of the vacuum electromechanical coupling rate between hybridized-mode and the mechanical resonator as the magnetic flux through the SQUID loop is increased, while $\omega_+ = 2\pi \times 6.025$ GHz is kept fixed. The maximum flux applied corresponds to a field of 3.7 mT. The blue-dotted line shows the expected coupling rate calculated from the device parameters. The error bars represent the uncertainty resulting from the numerical fit of the power spectral density.

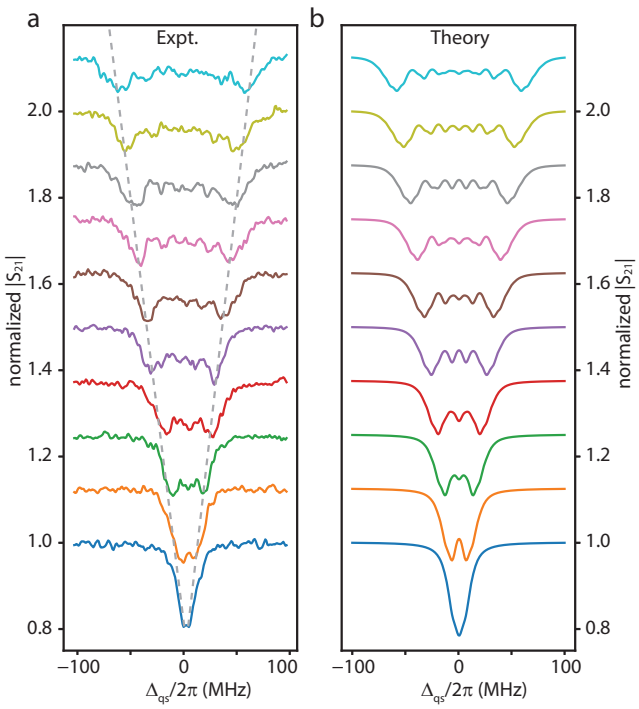

FIG. 4. (a) Measurement of the qubit spectrum with the detuning of spectroscopy tone $\Delta_{qs} = \omega_s - \omega_q$, where ω_s is the spectroscopy frequency. The mechanical drive signal is varied from 1 to 10 mV in steps of 1 mV (bottom to top). The Rabi flop rate $\Omega_R/2\pi$ is about 3 MHz. Apart from the primary splitting, weak fringes arising from the Landau-Zener-Stückelberg interference are visible. Dotted lines are added as guide to the eye. (b) Qubit spectrum calculated using the master equation. The qubit frequency deviation is changed from 7 MHz to 70 MHz in steps of 7 MHz (bottom to top). A qubit relaxation rate of 2 MHz, and a pure dephasing rate of 4 MHz is used to calculate the qubit spectrum. In both panels, the probe transmission corresponding to the lowest mechanical drive is normalized to one, and an offset of 0.125 has been added successively.

Figures

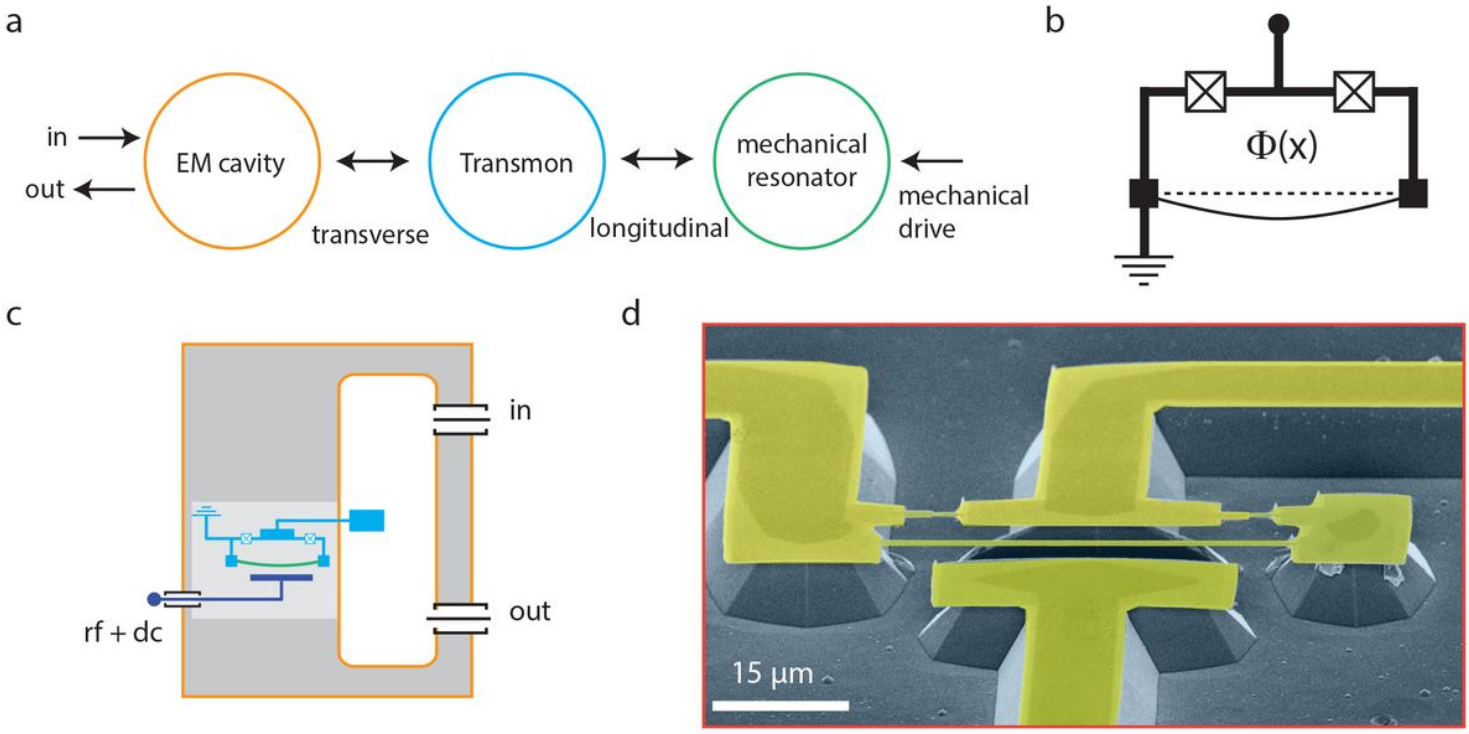

Figure 1

(a) A schematic showing various components of the hybrid electromechanical system. The transmon qubit couples to an electromagnetic (EM) cavity via the transverse coupling. A lowfrequency mechanical resonator couples to the transmon qubit via the longitudinal coupling. (b) A schematic of the SQUID loop with a suspended arm. Due to the magnetic ux Φ(x) dependence of Josephson inductance, it forms a displacement-dependent inductor. (c) A cross-sectional view of a 3D-cavity based transmon device. The gray (white) portion represents the copper (machined chamber). Input-output ports for microwave and a third port added for mechanical actuation is shown. The SQUID loop is placed inside a small recess of the cavity schematically shown by the lighter gray area. (d) A false-color SEM image of the SQUID loop, showing the suspended portion of the Josephson junctions and the nanobeam. The mechanical resonator has a length and width of 45 μm and 300 nm, respectively. It consists of a 50 nm coating of aluminum over 100 nm thick highly-stressed SiN lm. The T-shaped electrode in the lower-half of the image is used to actuate the mechanical resonator.

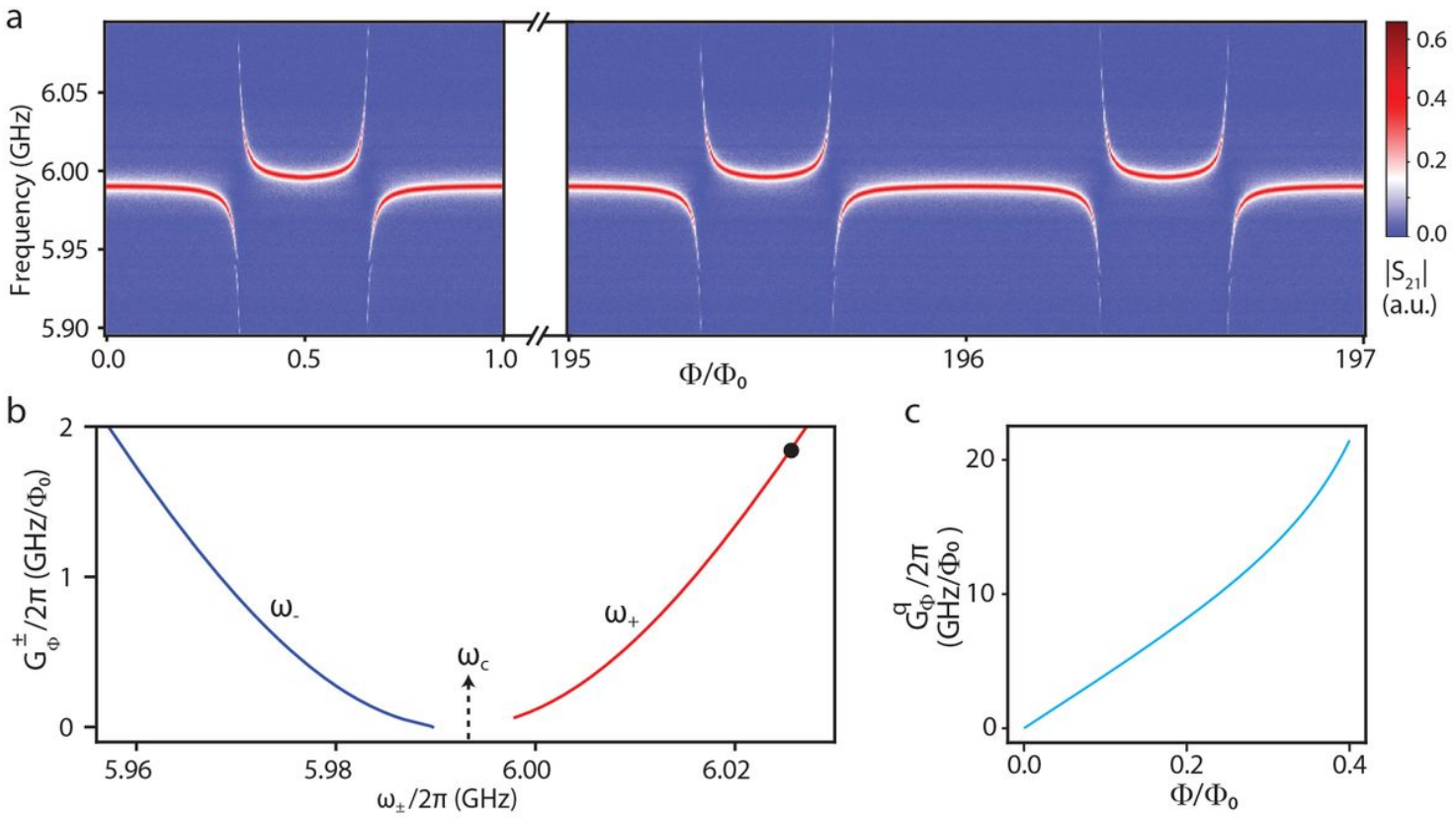

Figure 2

(a) Color scale plot of transmission |S21| through the cavity as the magnetic ux through the SQUID loop is varied. The strong qubit-cavity coupling (J) manifests as the avoided-crossing, yielding J ~ 2π x 85 MHz. The extension panel shows the trend of avoided crossing at larger values of the magnetic ux. (b) The flux-responsivity GΦ± = ∂ω±=∂Φ, computed using the measured device parameters, assuming identical junctions, plotted as a function of hybridized frequencies. The black dot denotes the operating point of 6.025 GHz, corresponding to GΦ+/2π ~ 1.8 GHz/Φ0 for the subsequent measurements. The arrow indicates the bare cavity frequency ωc/2π ~ 5.993 GHz. Panel (c) shows the flux-responsivity of uncoupled qubit GqΦ = ∂ωq/∂Φ with the magnetic flux.

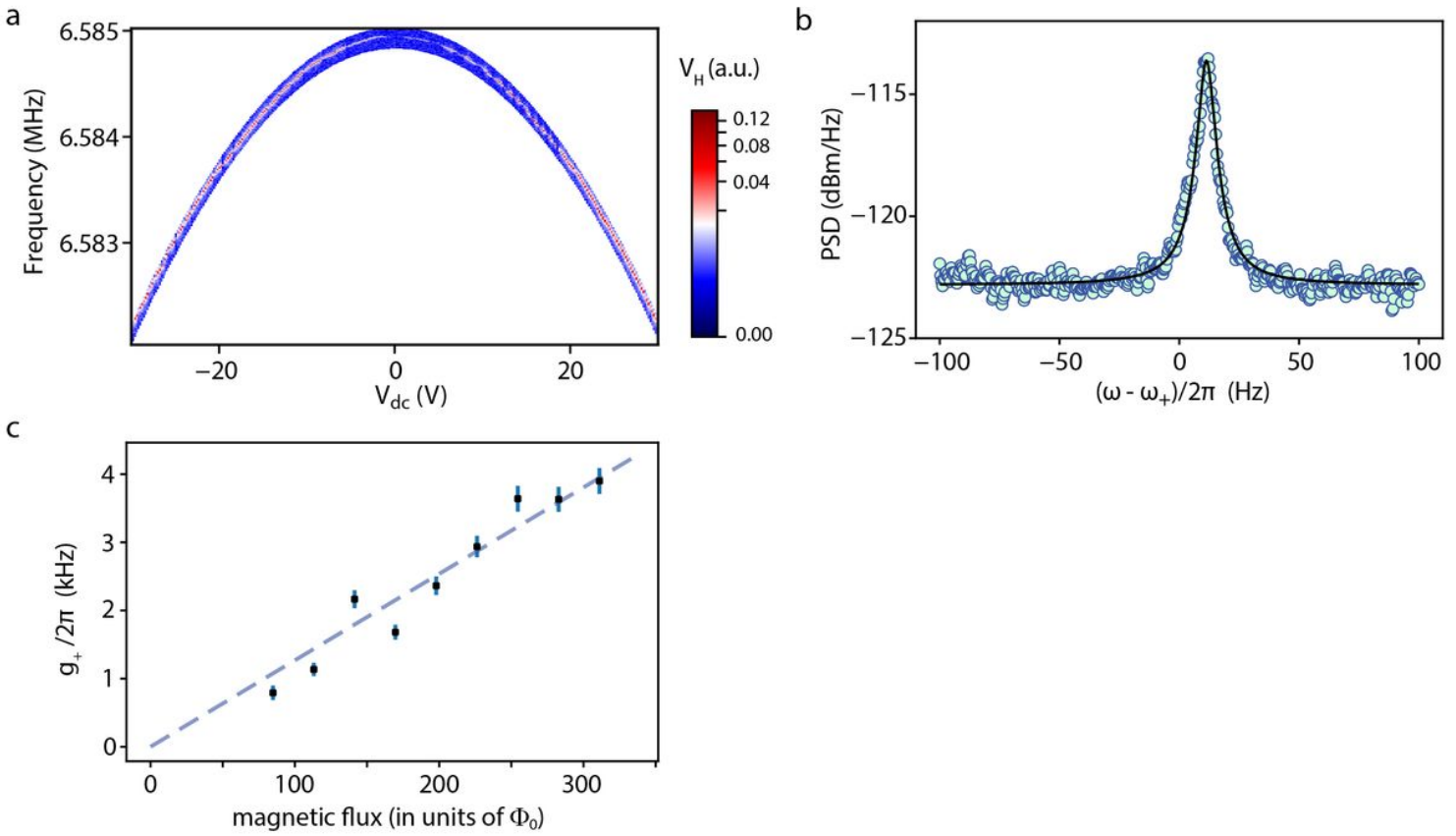

Figure 3

(a) Color plot of the mixed-down signal VH as mechanical actuation frequency and dc voltage is varied. The mechanical resonance appears as a sharp change in the color. Blue(red) color represents low(high) values of the signal. To reduce the total measurement time, the mechanical actuation frequency range is automatically adjusted to follow the mechanical mode. (b) Average PSD along with a fitted curve yielding a mechanical linewidth γm ~ 2π x 6 Hz corresponding to a quality factor of ~ 1:1 x 10^6. (c) Plot of the vacuum electromechanical coupling rate between hybridized-mode and the mechanical resonator as the magnetic flux through the SQUID loop is increased, while ω+ = 2π x 6:025 GHz is kept fixed. The maximum flux applied corresponds to a eld of 3.7 mT. The blue-dotted line shows the expected coupling rate calculated from the device parameters. The error bars represent the uncertainty resulting from the numerical t of the power spectral density.

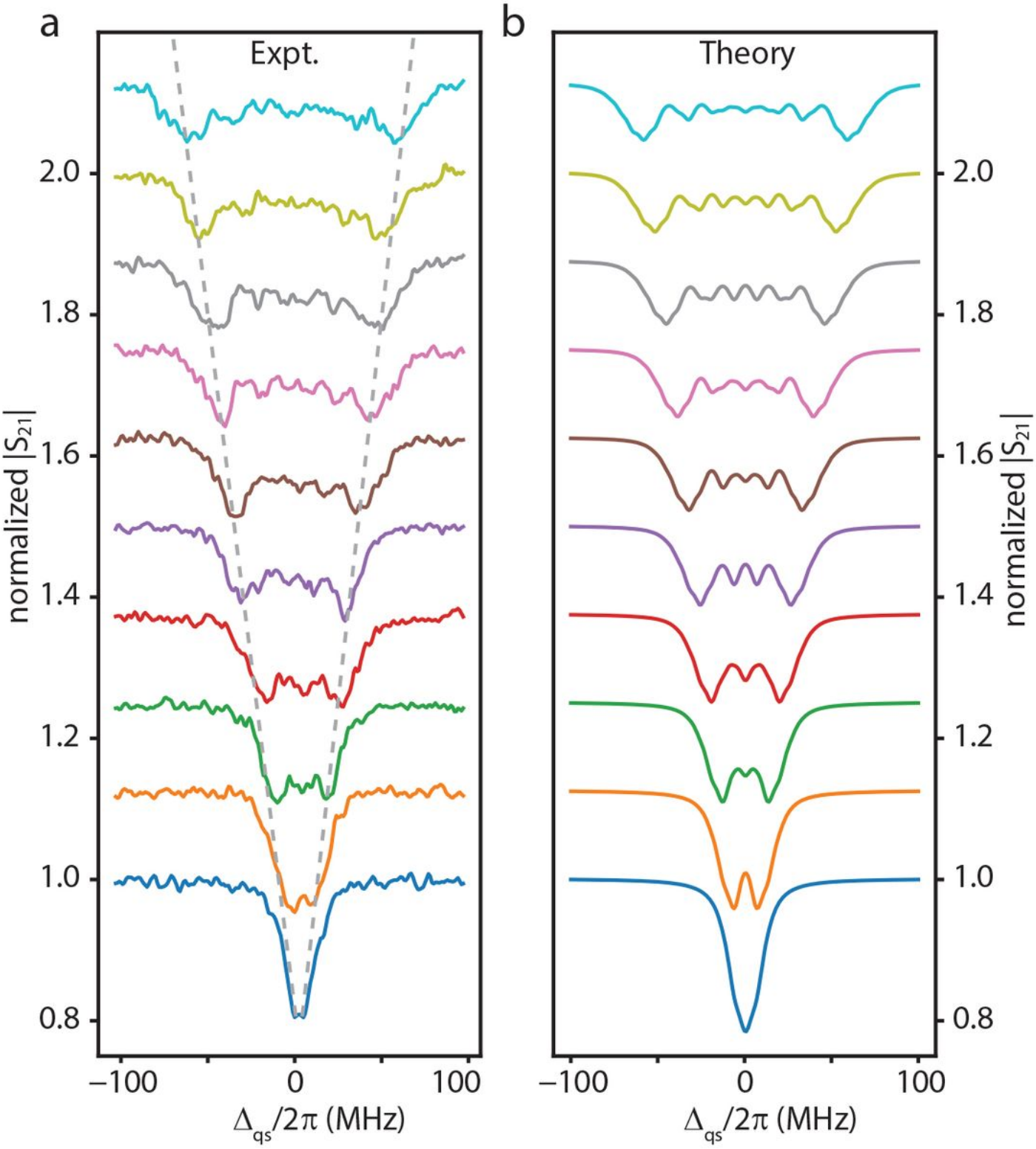

Figure 4

(a) Measurement of the qubit spectrum with the detuning of spectroscopy tone Δqs = ωs - ωq, where ωs is the spectroscopy frequency. The mechanical drive signal is varied from 1 to 10 mV in steps of 1 mV (bottom to top). The Rabi op rate ΩR=2π is about 3 MHz. Apart from the primary splitting, weak fringes arising from the Landau-Zener-St□uckelberg interference are visible. Dotted lines are added as guide to the eye. (b) Qubit spectrum calculated using the master equation. The qubit frequency deviation is

changed from 7 MHz to 70 MHz in steps of 7 MHz (bottom to top). A qubit relaxation rate of 2 MHz, and a pure dephasing rate of 4 MHz is used to calculate the qubit spectrum. In both panels, the probe transmission corresponding to the lowest mechanical drive is normalized to one, and an offset of 0.125 has been added successively.

Supplementary Files

This is a list of supplementary files associated with this preprint. Click to download.

- SupplementaryInformationlow.pdf